A&A 457, 157–166 (2006)
DOI: 10.1051/0004-6361:20054746

Astronomy & Astrophysics

HH135/HH136 – a luminous H_2 outflow towards a high-mass protostar⋆,⋆⋆

R. Gredel

Max-Planck Institut für Astronomie, Königstuhl 17, 69117 Heidelberg, Germany
e-mail: gredel@mpia.de

Received 21 December 2005 / Accepted 4 May 2006

ABSTRACT

Context. Molecular hydrogen observations towards Herbig-Haro objects provide the possibility of studying physical processes related to star formation.
Aims. Observations towards the luminous IRAS source IRAS 11101-5928 and the associated Herbig-Haro objects HH135/HH136 are obtained to understand whether high-mass stars form via the same physical processes as their low-mass counterparts.
Methods. Near-infrared imaging and spectroscopy are used to infer H_2 excitation characteristics. A theoretical H_2 spectrum is constructed from a thermal ro-vibrational population distribution and compared to the observations.
Results. The observations reveal the presence of a well-collimated, parsec-sized H_2 outflow with a total H_2 luminosity of about 2 $L_\odot$. The bulk of the molecular gas is characterized by a ro-vibrational excitation temperature of 2000 ± 200 K. A small fraction (0.3%) of the molecular gas is very hot, with excitation temperatures around 5500 K. The molecular emission is associated with strong [FeII] emission. The H_2 and [FeII] emission characteristics indicate the presence of fast, dissociative J-shocks at speeds of $v_s \approx 100$ km s^{-1}. Electron densities of n_e = 3500–4000 cm^{-3} are inferred from the [FeII] line ratios.
Conclusions. The large H_2 luminosity combined with the very large source luminosity suggests that the high-mass protostar that powers the HH135/HH136 flow forms via accretion, but with a significantly increased accretion rate compared to that of low-mass protostars.

Key words. ISM: individual objects: HH135 – ISM: individual objects: HH136 – ISM: Herbig-Haro objects – ISM: jets and outflows

1. Introduction

Near-infrared studies of molecular hydrogen emission in Herbig-Haro (HH) objects provide a powerful tool to gain insight in the physical processes that occur during the early phases of low-mass star formation. The total H_2 luminosities are proportional to the accretion rates in the early phases of the protostellar evolution (Stanke 2000; Froebrich et al. 2003), and the H_2 ro-vibrational population distribution allows us to determine the physical scenarios that are at work in the supersonic jets that form during the accretion phase (McCoey 2004, and references therein). A complementary tool to study such regions is available via the near-infrared emission lines of [FeII] and other atomic emission lines, that allow us to measure electron densities in the shocked material (e.g., Nisini et al. 2002).

In a number of HH objects, and most prominently in HH objects that show pronounced [FeII] emission, a temperature stratification is inferred from the H_2 observations, where part of the molecular gas reach temperatures above 5000 K (Giannini et al. 2004). The combined H_2 and [FeII] emission has been explained in terms of fast J-type shocks, where the [FeII] emission is produced in dissociative parts of the shocks, and where H_2 arises in the slower, non-dissociative regions (e.g., Gredel 1994). Detailed model calculations of J-type shocks with magnetic precursors confirm such a model, and produce population distributions where the rotational excitation temperatures increase with increasing vibrational state of H_2 (e.g., Flower et al. 2003). C-type shocks at largely different physical conditions produce similar H_2 population distributions, however, and the H_2 population distribution alone does not allow us to distinguish between both scenarios (Flower et al. 2003). The presence of [FeII] emission is generally interpreted in terms of dissociative J-type shocks, although it is conceivable that C-type shocks produce [FeII] as well (Le Bourlot et al. 2002).

Near-infrared studies of outflows from intermediate- and high-mass star forming regions are rare, either because such outflows are not very frequent per se or because high-mass star-forming regions are deeply embedded in general. Some outflows that are observed from high-luminous sources such as Orion (10^5 $L_\odot$) lack the high degree of collimation that is typical for outflows from low-mass star-forming regions. Other flows that emerge from luminous IRAS sources, such as HH80/81 (2×10^4 $L_\odot$, Martí et al. 1995), IRAS 16547-4247 (6×10^4 $L_\odot$, Brooks et al. 2003), or IRAS 18151-1208 (2×10^4 $L_\odot$, Davis et al. 2004), are highly collimated. It is not clear whether intermediate- and high-mass stars form in a similar way to low-mass stars, but with enhanced accretion rates, or whether different processes, such as the merging of low-mass protostars, are at work. Enlarging the sample of near-infrared observations of regions of intermediate- and high-mass star formation and comparing the general properties of their H_2 and [FeII] emission with those of low-mass star-forming regions is therefore desirable.

In the following, a study of the molecular outflow HH135/HH136, which is powered by the cold and very luminous

⋆ Based on observations collected at the European Southern Observatory, La Silla, Chile.
⋆⋆ Appendix A is only available in electronic form at http://www.edpsciences.org

(10^4 $L_\odot$) IRAS source IRAS 11101-5928, is presented. The pair of Herbig-Haro objects HH135/HH136 was discovered by Ogura & Walsh (1992) in an objective prism survey and is located in the bright rimmed cloud No. 64 of Sugitani & Ogura (1994) in the Eastern Carina region. The HII region, also known as Gum 36, is believed to be excited by the open cluster Stock 13, for which photometric distances of 2.7 kpc are available (Steppe 1977). The general morphology of HH135/HH136 indicates that the two objects are formed at the opposite flow directions of a bipolar flow, which is driven by IRAS 11101-5829. The velocity field of the HH135/HH136 region is complex, however, and the fact that the main part of the emission from both HH135 and HH136 is blue shifted led Ogura & Walsh (1992) to conclude that HH135 and HH136 form two different, independent flows. Near-infrared *JHK* polarimetric observations of the associated reflection nebula carried out by Tamura et al. (1997) showed that IRAS 11101–5829 is the only illuminating source of the nebula that is associated with HH135/HH136. A more recent millimetre study by Ogura et al. (1998) presented a model that explains the observed velocity features and where HH135 and HH136 form part of a single, bipolar flow driven by IRAS 11101-5829. This view is supported by the very recent polarimetric observations by Chrysostomou et al. (2005), who proposed that a strong helical magnetic field threading though HH135/HH136 maintains the strong collimation of the flow.

The purpose of this paper is to investigate the molecular hydrogen emission of HH135/HH136, and to study how the emission characteristics differ from those of low-mass star-forming regions. The observations are presented in Sect. 2, which also includes a more detailed discussion of the data reduction method and errors. The imaging results are given in Sect. 3.1 and the spectroscopy in Sect. 3.2. Section 3.3 contains an analysis of the global properties of the molecular hydrogen emission, and Sect. 3.4 summarises the results of an analysis derived from the [FeII] lines, which are observed towards HH135/HH136. The main conclusions of this study are summarized in Sect. 4.

2. Observations and reduction

Near-infrared imaging and spectroscopy of the HH135/HH136 complex was carried out in March 1999 and February 2004 at the La Silla Observatory, using SOFI at the New Technology Telescope (NTT). Images were obtained at both epochs in three narrow-band filters *NB164*, *NB212*, and *NB228*, using a pixel scale of 0.″144/px. Central wavelengths are 1.644 μm, 2.124 μm, and 2.280 μm, respectively, and widths are 0.025 μm, 0.028 μm, and 0.030 μm, respectively, for the *NB164*, *NB212*, and *NB228* filters, according to the information given in the ESO web pages. Dithered images were used to construct background subtracted images, including corrections for sky, dark-current, and bias. This method assumes that the background is constant and does not vary across an image, which is not the case in the *H*-band. All images were re-centered to a common reference, but no effort was made to correct for field distortion across the image.

In March 1999, spectroscopic observations were obtained along three slit positions using the red grism GR in order 1, covering the 1.52–2.52 μm wavelength region. The slit was set to a width of 0.″6, and measurements of the width of individual spectral lines showed that an effective spectral resolution of $R = \lambda/\Delta\lambda = 550$ was achieved. Spectroscopic observations were also carried out in February 2004, using the blue grism GB in order 1 and a slit of 0.″6, covering the 0.94–1.60 μm wavelength region at a spectral resolution of $R = 850$. Additional spectra were gathered using the HR grism in orders 3 and 4, covering the 2.0–2.3 μm and 1.5–1.8 μm wavelength regions, respectively. The *K*- and *H*-band observations obtained with the HR grism were carried out with a slit width of 0.″6 as well. Spectral resolutions, as obtained from the width of the emission lines, were $R = 1066$ and $R = 1600$, respectively. Explicit `sky` frames were obtained by moving the object along the slit. This is possible because the infrared emission of HH135/HH136 is extended over about 1 arcmin, compared to the total slit length of 5 arcmin.

The spectroscopic observations were reduced using the MIDAS `long` package. The long-slit spectra suffer from a pronounced curvature of the spectral lines perpendicular to the dispersion direction, and the distorted 2-D frames were rectified by use of a second-order polynomial. Pixel units along the dispersion direction were then transformed into a linear wavelength scale by the use of xenon-argon calibration frames. A first-order background subtraction was obtained by building (`object - sky`) difference frames. Short-term temporal and spatial variations at scales comparable to the length of the slit result in residuals in the background in a large number of the difference frames. A second-order sky subtraction was achieved via the standard technique of extracting the positive and negative spectra from the difference frames and adding them in the correct sense. Extraction windows to obtain the 1-D spectra from the 2-D difference frames were typically 12 pixels along the slit. On the spatial scale of 0.″29/px, the extraction windows correspond to solid angles Ω of about 2 arcsec^2 on the sky or $\Omega = 5 \times 10^{-11}$ sr. The atmospheric transmission was determined via observations of standard stars at slit widths of 0.″6. Stellar fluxes were measured with a second integration, but slits opened to 2″ to minimise slit losses. During the observations, the seeing varied from 0.″5 to 1.″5. In phases of poor seeing, the flux conversion factors determined from the stellar observations varied by up to 30%. The highly peaked nature of the line emission in some of the knots, combined with positional errors in the slit position for the various grism settings and the narrow slit of 0.″6 adopted here, causes differences in the reported fluxes towards some of the knots that reach, in the worst cases, a factor of about three (cf. Tables A.3 and A.4). This is well illustrated in Fig. 8, which shows that an error of less than 0.″5 in the position of the slit would cause the loss of most of the flux in knot B1. The consequences of these kinds of flux uncertainties for the analysis of the H_2 and atomic emission lines in HH135/HH136 are discussed in detail in Sects. 3.2 and 3.4. The tables of Pickles (1998) were used to convert the counts of the standard stars to flux units.

In addition to the near-infrared observations, optical images in the [SII] ($\lambda_{\rm center}$ = 673 nm, $FWHM = 6$ nm) and Gunn z($\lambda_{\rm cut\text{-}on}$ = 840 nm) were obtained in April 1993, using EFOSC2 at the 2.2 m telescope and CCD#19. Integration times were 300 s in [SII] and 2100 sec in Gunn z.

3. Results and discussion

The narrow-band [SII] image of the HH135/HH136 region and the Gunn z image are shown in Figs. 1 and 2. The observations were obtained during an atmospheric seeing of about 1.″3. The image was re-binned to a pixel scale of 0.″144 to allow for a comparison with the near-infrared images described below. The optical knots in the [SII]-image are labeled following the notation of Ogura & Walsh (1992). A continuum subtracted image constructed by use of the Gunn z image shows that the optical knots HH136-E (IRS9 in the notation of Tamura et al. 1997), HH136-I, and HH136-J are continuum sources with weak if any

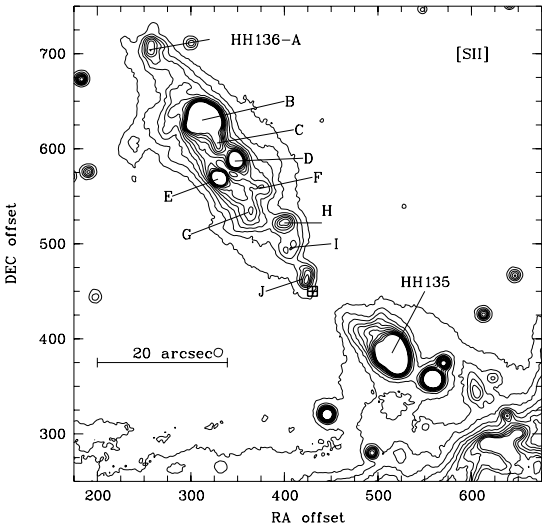

Fig. 1. [SII] image of HH135/HH136 and part of the G 36 region in Carina. Optical knots in HH136 are labeled following the notation by Ogura & Walsh (1992). The crossed square south of knot J marks the position of the IRAS source IRAS 11101-5829. North is up and east is left.

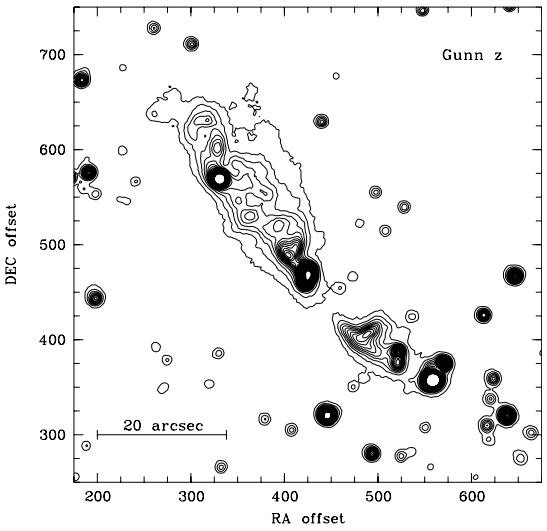

Fig. 2. Gunn z image of HH135/HH136.

[SII] emission. Strong but featureless [SII]-emission occurs towards HH135. The [SII] emission at the southern boundary of the imaged region traces the bright rim of Sugitani 64.

3.1. Near-infrared imaging of HH135/HH136

Narrow-band images obtained in the NB212, NB164, and NB228 filters are shown in Figs. 3–5, respectively. The slit locations shown in Fig. 3 are those adopted during the February 2004 observations and correspond to position angles of 33°, 43°, and 45°. Figure 4 includes the slit locations for the March 1999 spectroscopic observations, at position angles of 34.°5, 38°, and 45°. Observations at a position angle of 34.°5 were repeated twice. The NB228 passband does not cover any strong emission lines and was used to construct the continuum-subtracted images in the H_2 2.122 μm and [FeII] 1.644 μm lines. A scaling factor of 0.933 that corresponds to the ratio of the filter widths was applied to the flux in NB228 to obtain the H_2 image shown in

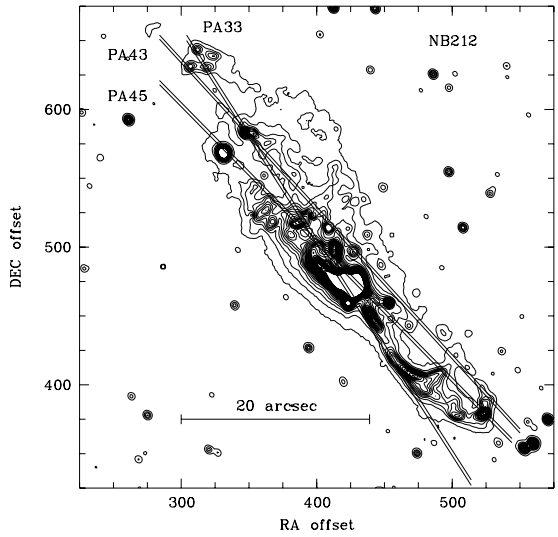

Fig. 3. Narrow-band image of the HH135/HH136 region obtained in the NB212 filter, which is centered on the (1, 0) $S(1)$ H_2 emission line near 2.12 μm. The three double lines indicate slit locations and slit widths for the February 2004 spectroscopic observations, with position angles of PA = 33°, 43°, and 45°. North is up and east is left.

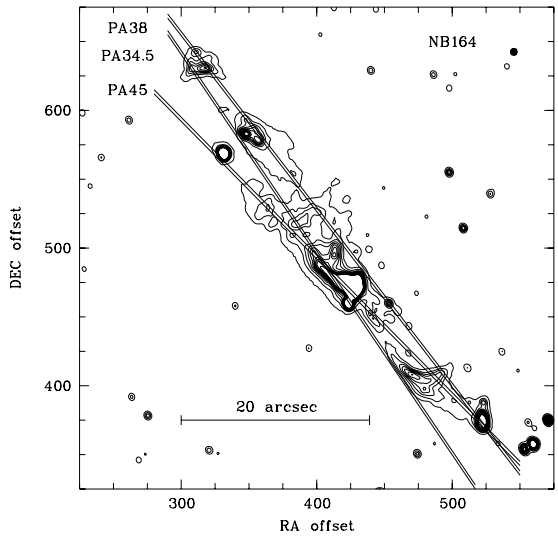

Fig. 4. Narrow-band image of the HH135/HH136 region obtained in the *NB164* filter, which is centered on the wavelength of the [FeII] $a^4D_{7/2}$–$a^4F_{9/2}$ emission line near 1.644 μm. The three double lines indicate slit locations and slit widths for the March 1999 spectroscopic observations, with position angles of PA = 34.°5, 38°, and 45°. North is up and east is left.

Fig. 7. In a similar way, the continuum-subtracted [FeII] image shown in Fig. 6 was constructed using a scaling factor of 0.3.

The overall morphology of the H_2 emission in the HH135/HH136 region is that of a highly collimated bipolar flow with various H_2 emission knots along the flow direction. The labeling of the infrared H_2 knots of Fig. 7 follows the notation of the optical knots in the [SII] image. This is possible because in general, the overall morphology of the [SII] and the H_2 emission is very similar. Exceptions occur for the optical knots HH136-A, C, and F, which do not have near-infrared counterparts in H_2 or [FeII], and which do not show significant infrared continuum emission either. The optical knot HH136-B splits up into four point-like objects, B1–B4. At the NE prolongation of knots B1 and B2, the diffuse H_2 emission labeled

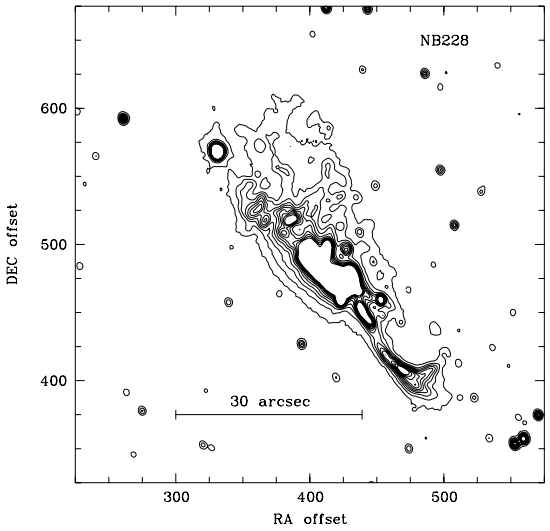

Fig. 5. Narrow-band image of the HH135/HH136 region obtained in the *NB228* filter. North is up and east is left.

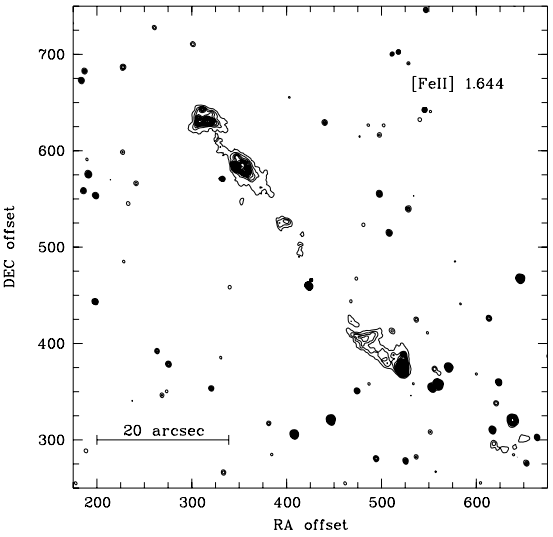

Fig. 6. Continuum-subtracted image showing the [FeII] 1.64 μm emission towards HH135/HH136.

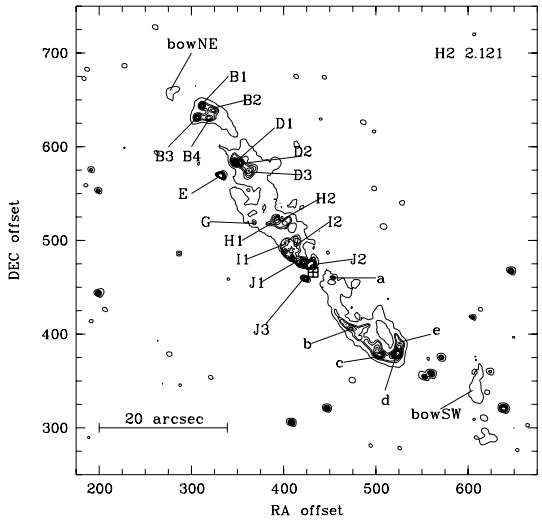

Fig. 7. Continuum-subtracted image showing the H_2 2.122 μm emission towards HH135/HH136. The strongest knots are labeled.

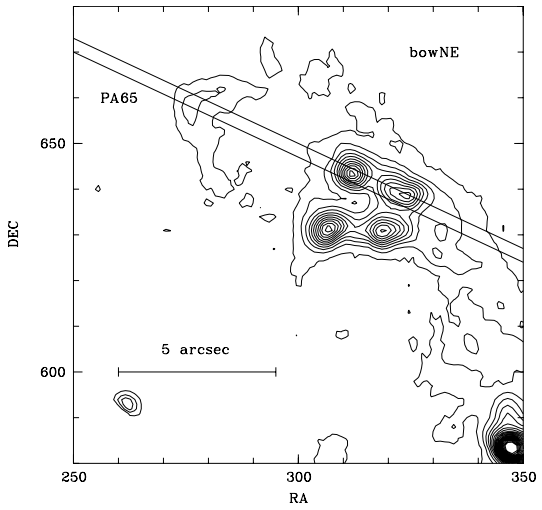

Fig. 8. Morphology of the molecular hydrogen emission at the NE extreme of the HH135/HH136 flow. The double lines indicate the position of a slit and its width placed at a position angle of PA = 65°.

bow-NE has a pronounced bow-shaped morphology that suggests a B2-bowNE flow direction. Knots D1-D3 (optical knot HH136–D) show strong H_2 emission with weak underlying continua. Knot E is a strong continuum source (IRS-9 in the notation of Tamura et al. 1997) without pronounced H_2 emission. The region between infrared knots G-J2 contains a large number of infrared continuum sources, and very strong infrared continuum emission occurs between knots H1-J2 (cf. Fig. 5). In the NB228 continuum image shown in Fig. 5, the presence of a large number (30–40) of point-like continuum sources is discerned, in agreement with the finding of Tamura et al. (1997) based on their K_s image. The slit traces shown in Figs. A.1 and A.2 show that most of the continuum sources that are located between knots I1–J3 show H_2 emission as well. Knots J1–J3 are very strong continuum sources. Because of the very strong continuum emission between I1–J3, a proper continuum-subtracted H_2 image for that region could not be constructed. It is noted that between knots J2 and d, a remarkably circular shape of very faint H_2 emission is discerned in a false-color image, with knot b at the southeastern and knot a at the northeastern extremes of this "cavity".

Five infrared knots here labeled a–e are identified in HH135. The H_2 emission of HH135 has a morphology of a bow with an apex near knot d and wings formed by knots b, c, and e. At the SW prolongation of the HH136-HH135 complex, the diffuse H_2 emission labeled bow-SW has a pronounced bowshape. Faint H_2 emission also occurs in the SW extreme of HH135. The emission has a pronounced bow morphology as well. The H_2 continuum-subtracted image is reproduced in Fig. 9. The bow morphology, which cannot be demonstrated too convincingly in the contour plot shown here, is more apparent in a false-color H_2 image. The whole extent of the collimated molecular hydrogen flow is 80″, which corresponds to about 1 parsec at a distance of 2.7 kpc.

The morphology of the [FeII] emission is given in Fig. 6. The [FeII] emission is, in general, very strong, and it is associated with molecular hydrogen emission, Exceptions occur for bow-NE and bow-SW, which show faint [FeII] emission only. The very strong [FeII] emission near knot d is displaced by a few arcsec towards the SW relative to its H_2 counterpart. The displacement between the [FeII] and H_2 emission provides evidence for the presence of fast, dissociative J-type shocks with

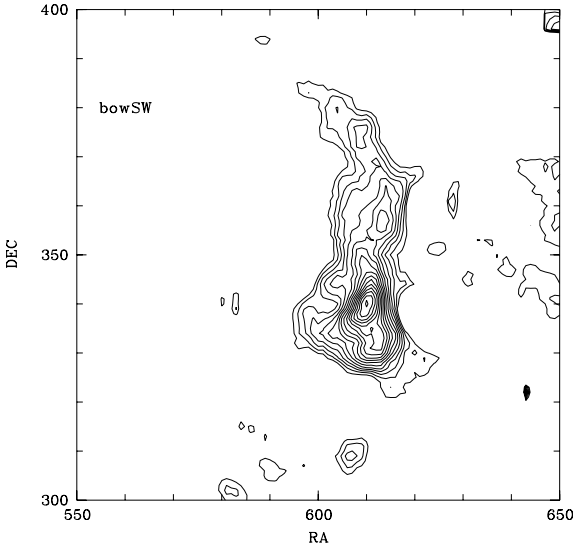

Fig. 9. Morphology of the molecular hydrogen emission at the SW extreme of the HH135/HH136 flow.

a NE-SW flow direction, where the [FeII] emission arises in the fast, dissociative parts of the shocks, such as the apex of a bow shock, and where H_2 arises in slower regions or in oblique shocks, such as those in the wings of a bowshock.

The NE-extreme of the HH135/HH136 flow is shown in Fig. 8, together with the location of a slit at position angle PA = 65°, which was used in February 2004 to obtain spectra of objects bowNE and knots B1 and B2. The image shows the continuum-subtracted H_2 emission. Object bowNE has a pronounced bow shape with knots B1 and B2 located along a possible SW-NE flow direction. The alignment of bowNE-B2 differs by some 20° from the large-scale alignment of the HH135/HH136 complex, which suggests the presence of a second flow, that is not powered by IRAS 11101-5829.

The images shown in Figs. 4–7 were obtained in February 2004 at a seeing of 0.″55. Seeing during the March 1999 imaging campaign was significantly worse and generally above 1 arcsec. A comparison of the images obtained at both epochs does not show any spatial displacement of the various knots, which supports the assumption that HH135/HH136 is located at the large distance of 2.7 kpc. Thus, no effort was made to obtain proper motions and displacement vectors from both epochs.

3.2. Molecular hydrogen excitation across the HH135/HH136 flow

During the March 1999 and February 2004 observing campaigns, spectra of the HH135/HH136 complex were obtained using a total of 7 slit positions at various position angles across the region. The relatively large number of slit positions was adopted to investigate possible changes in the H_2 excitation across the HH135/HH136 flow. The variation of the flux in the (1, 0) $S(1)$ line of H_2 along the various slit positions is shown in Figs. A.1, A.2. The individual emission knots, as identified in Fig. 7, are marked in these slit traces. The bold lines represent the flux variation in the continuum along the slit. It can be seen that many of the H_2 emission line knots coincide with faint, underlying continuum sources. The H- and K_s-band spectra are shown in Figs. A.3 and A.4. Note the very strong continuum emission that is associated with knots H1 and I2.

Tables A.1–A.4 contain the unreddened line fluxes measured towards the various knots. From the analysis of the [FeII] emission lines, a visual extinction of $A_V = 2.7$ mag is inferred (cf. Sect. 3.4) and was used to obtain the population densities $N(v'J')$ in the ro-vibrational levels $v'J'$. $A(v'J'v''J'')$ and $\bar{\nu}$ are the transition probabilities and wave numbers, respectively. The visual extinction obtained from the [FeII] lines is in excellent agreement with the values of $A_V = 2.8-3.1$ mag obtained by Ogura & Walsh (1992) from their optical spectroscopy. The population densities were used to construct excitation diagrams for the various knots, where values of $\ln(N(v'J')/g$ are plotted versus excitation energies $E(v'J')$ of the ro-vibrational levels. Statistical weights are $g = g_s(2J' + 1)$, where the nuclear-spin statistical weights g_s are 1 and 3 for even and odd rotational levels J', respectively. The above analysis implies that the H_2 ortho/para ratio is 3, which in J-type shocks is attained at shock velocities above $v_s \approx 15$ km s^{-1}, or $v_s > 40$ km s^{-1} for C-type shocks (Wilgenbus et al. 2000).

The excitation diagrams for the various knots are shown in Fig. 10. Open triangles and open squares correspond to data inferred from the blue and red grisms GB and GR, respectively, while filled triangles and squares represent data inferred from the H- and K-band observations carried out at the higher spectral resolution, respectively. Straight lines fitted to the various population distributions show single temperature fits, with values of 1650 K for knot c, 1815 K for knots b and B2, 1855 K for knot B4, 1920 K for knots B1, B3, D1, D3 and H1, 2030 K for knot d and bowNE, and 2160 K for knot I2. Uncertainties in the derived excitation temperatures are about 200 K. The temperature range among the various knots is extremely narrow, and except for knot c, all data are consistent with a constant excitation temperature of 2000 ± 200 K.

In a few cases, the population densities inferred from the various grism settings for a given knot are not consistent with each other. This is seen in the excitation diagrams of Fig. 10, where most pronounced discrepancies occur for knots B1, D1, and c. For knot B1, population densities derived from the GB observations are lower by factors of a few compared to population densities derived from GR and the H and K_s grisms. For knots D1 and c, population densities derived from the observations with the GR grism are too low, if compared with the population densities derived from the GB, H, and K_s observations. The discrepancies do not arise from a larger than assumed reddening towards these knots, which would explain the differences in knot B1, but not those in D1 and c. They result from relatively severe slit losses during phases of poor seeing and from positional differences in the various grism settings, most pronounced for the GB and GR observations that were taken several years apart. However, the temperatures derived from the discrepant population densities agree with temperatures derived from the remaining data, for a given knot. This is illustrated by the dashed lines shown for knots B1, D1, and c, which are temperature fits to the discrepant population densities. Thus, discrepancies do not in any way affect the conclusions derived here concerning the H_2 excitation, but they severely hamper a more detailed analysis of the [FeII] emission as discussed below.

3.3. Global properties of the H_2 emission in HH135/HH136

As demonstrated in Fig. 10, the ro-vibrational population distribution of H_2 among the various knots is remarkably similar. It thus makes sense to sum up the individual spectra to increase the signal-to-noise ratio, to search for fainter H_2 emission lines that

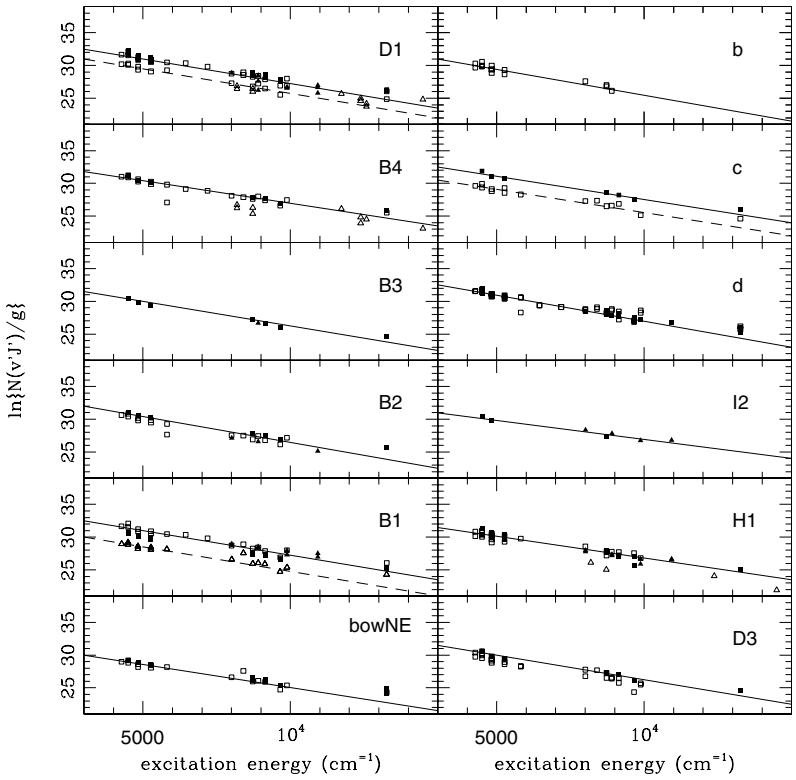

Fig. 10. Excitation diagrams constructed for individual knots in HH135/HH136 with values of $\ln(N(v'J')/g$ plotted versus excitation energies $E(v'J')$. Open triangles and open squares correspond to data inferred from the blue and red grisms GB and GR, respectively, while filled triangles and squares represent the data inferred from the *H*- and *K*-band observations using the high-resolution grism. Straight lines correspond to single temperature fits to the population distribution, whereas dashed lines plotted in the diagrams of knots B1, D1, and c are fits to discrepant measurements (see text).

are not apparent in the individual spectra. This method simulates spectroscopic observations of HH135/HH136 with a very large aperture, and is thus physically meaningful. The sum spectra, shown in Figs. 12–16, show a wealth of additional, faint emission lines, particularly in the *J*-band. Some H_2 emission lines are identified explicitly in the figures. The importance of *J*-band observations for a proper characterization of the H_2 excitation has been emphasized by Giannini et al. (2002), and full use of the additional J-band emission lines is made here.

The H_2 line fluxes derived from the sum spectra and the inferred column densities $N(v'J')$ are given in Tables A.5–A.7. The conversion of molecular hydrogen fluxes to population densities was achieved via the relation $I(v'J'v''J'') = \frac{hc}{4\pi}\bar{\nu}A(v'J'v''J'')N(v'J')$. Intensities $I(v'J'v''J'')$ are inferred from the de-reddened fluxes $F(v'J'v''J'')$, using the solid angles Ω given in Sect. 2. The corresponding H_2 excitation diagram is shown in Fig. 11. The population distribution indicates the presence of a thermalized gas at $T_{\rm ex} = 2000$ K, which contains a minor fraction of 0.3% of hot gas at $T_{\rm ex} = 5500$ K. Dots in the excitation diagram show the modeled population densities in all levels at such a gas mixture.

Because of the wealth of [FeII] and other atomic emission lines in the spectra, and because of the relatively low spectral resolution, the confusion limit is reached in various spectral regions and care needs to be exercised when inferring line fluxes of individual emission lines. It thus makes sense to calculate a theoretical H_2 spectrum and compare it with the observed spectrum. This allows us to judge whether the fluxes of the molecular hydrogen lines listed in Tables A.5–A.7 are severely affected from line blends. A theoretical H_2 spectrum was constructed for thermalized H_2 in a gas mixture of 2000 K and 5500 K with a column density ratio of 300:1, using the code of Gredel & Dalgarno (1996). The theoretical spectra, calculated for a visual extinction of $A_{\rm V} = 2.7$ mag, were normalized to the strength of the (1, 0) $S(1)$ line and convolved with a Voigt profile at the

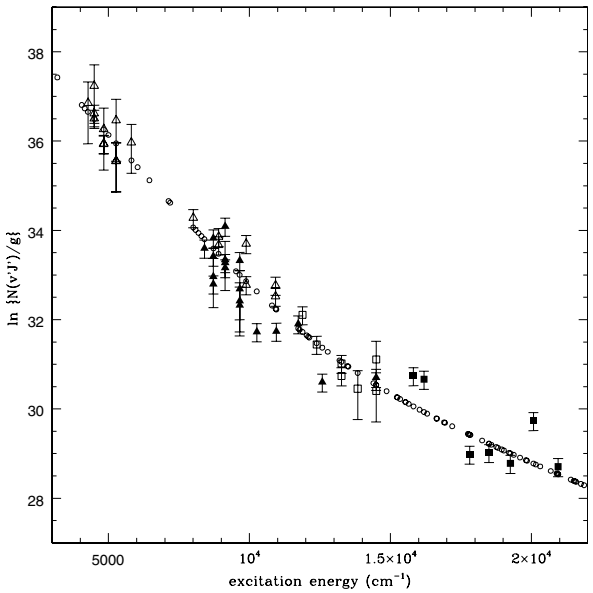

Fig. 11. Excitation diagram constructed from the H_2 sum spectra. Triangles, squares, and hexagrams, respectively, represent population distribution among rotational levels of $v' = 1$, 2, 3, and 4. Dots represent a theoretical population distribution constructed for a thermalized gas at a temperature of 2000 K, with a second component added at a temperature of 5500 K and a column density 300 times less than the first.

various spectral resolutions of the observed spectra. The theoretical spectra are reproduced in Figs. 12–16 as bold lines.

The comparison of the observations with the model spectra show that for single lines that appear unaffected by blends with atomic lines, the fit is excellent. The H_2 line fluxes in the *H*- and *K*-band atmospheric windows are generally very well reproduced (cf. Figs. 15 and 16). Note that the (1, 0) $S(1)$ line

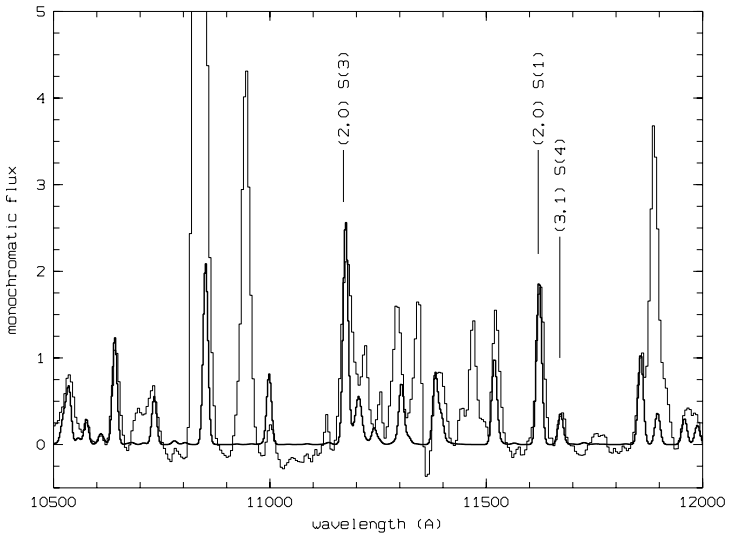

Fig. 12. Monochromatic fluxes versus wavelength of the sum spectrum including the model H_2 spectrum (bold line). The sum spectrum is obtained from individual spectra using grism GB. A few H_2 lines are identified.

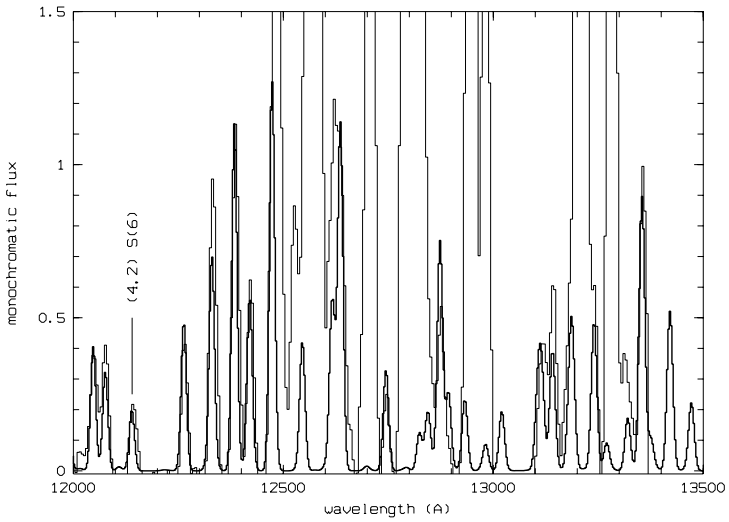

Fig. 13. Monochromatic fluxes versus wavelength of the sum spectrum including the model H_2 spectrum (bold line). The sum spectrum is obtained from individual spectra using grism GB. The (4, 2) $S(6)$ transition of H_2 is identified.

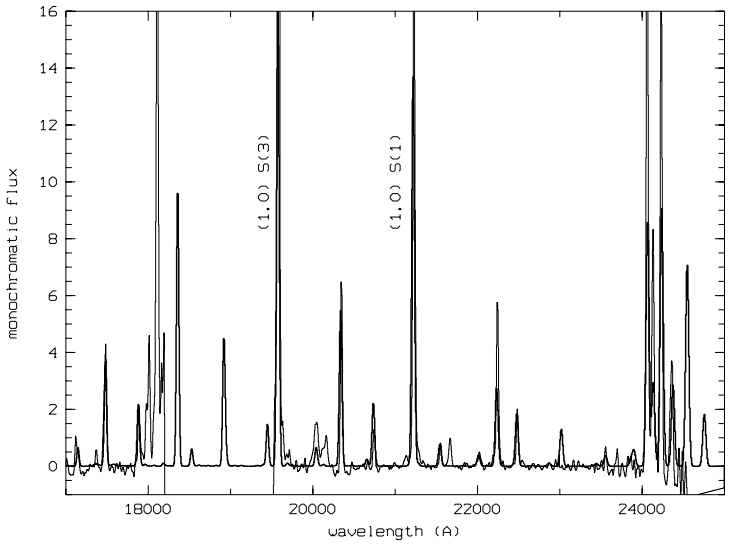

Fig. 14. Monochromatic fluxes versus wavelength of the sum spectrum including the model H_2 spectrum (bold line). The sum spectrum is obtained from individual spectra using grism GR. The (1, 0) $S(1)$ and (1, 0) $S(3)$ lines of H_2 are identified.

near 2.121 μm, as well as the $a^4D_{7/2}$–$a^4F_{9/2}$ [FeII] line near 1.644 μm, show broad emission wings. In the heavily crowded J-band spectra, individual H_2 lines that are free of blends are very well reproduced as well. Examples are the (2, 0) $S(1)$ and (3, 1) $S(4)$ pair near 1.164 μm (Fig. 12) and the (4, 2) $S(5)$, (4, 2) $S(6)$, and (2, 0) $Q(1)$–$Q(4)$ lines at 1.21–1.25 μm (Fig. 13). The very good fit of emission lines from $v' = 2$ to $v' = 4$ shows that the two-temperature fit to the H_2 population distribution (Fig. 11) is accurate, despite the flux uncertainties in many of the H_2 line fluxes that result from line blends.

Re-forming molecular hydrogen in the cooling, post-shock regions causes a pronounced variation in the population densities

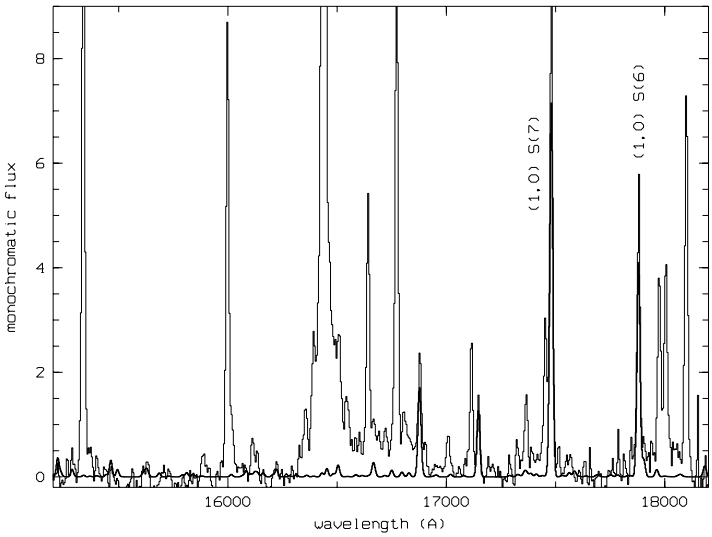

Fig. 15. Monochromatic fluxes versus wavelength of the sum spectrum including the model H_2 spectrum (bold line). The sum spectrum is obtained from individual spectra using the HR grism. The (1, 0) $S(6)$ and (1, 0) $S(7)$ lines of H_2 are identified.

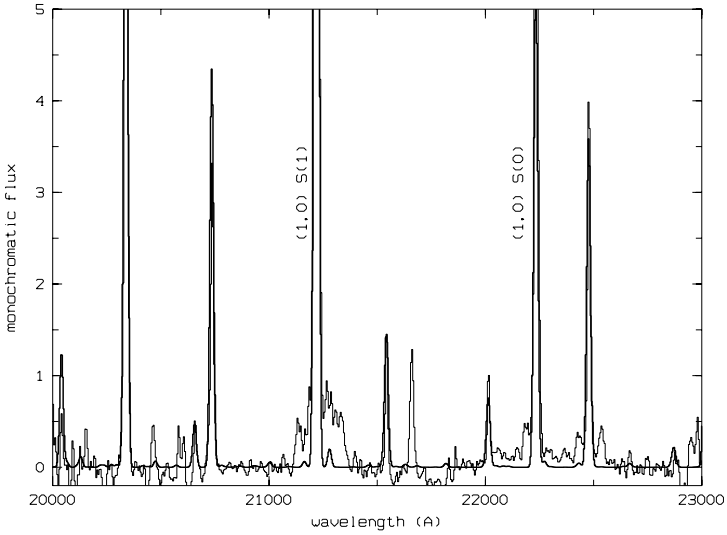

Fig. 16. Monochromatic fluxes versus wavelength of the sum spectrum including the model H_2 spectrum (bold line). The sum spectrum is obtained from individual spectra using the HR grism. The (1, 0) $S(0)$ and (1, 0) $S(1)$ lines of H_2 are identified.

of ro-vibrational levels with similar excitation temperatures, but different vibrational quantum numbers (e.g., Flower et al. 2003, their Fig. 6). The effect leads to a pronounced overpopulation of rotational levels in $v' = 0$, relative to levels in $v' = 1$ of similar excitation energy. Emission lines that arise from $v' = 0$ are not available in the present study. The rotational population densities in $v' = 0$ are very sensitive to C-type shocks, which produce very large column densities in these levels. C-type shocks have been used to explain the observed H_2 in various outflow sources, such as HH 99 and VLA 1623A (Davis et al. 1999) or in IRAS 18151-1208 (Davis et al. 2004). Others have used C-type shocks with magnetic precursors (McCoey et al. 2004; Flower et al. 2003). The lack of kinematical data and the lack of observations of H_2 emission from $v = 0$ makes it difficult to judge whether C-type shocks are relevant for the H_2 excitation in HH135/HH136, although they must not be ruled out.

For a gas mixture of warm molecular gas at 2000K plus a fraction of 0.3% at 5500 K, the model calculation produces a total H_2 flux of $F_{\rm tot}(H_2) = \Sigma_{v'J'v''J''} F(v'J'v''J'') = 14.2 \times F(1301)$, where $F(1301)$ is the flux in the (1, 0) $S(1)$ line and where the summation is carried out over all possible emission lines that arise from the E2 cascade in the $X^1\Sigma_g^+$ electronic ground state of H_2. The various slit positions employed here sample a total H_2 flux of $F_{\rm tot}$ $(H_2) = 1.2 \times 10^{-15}$ W m^{-2}, which corresponds to a total measured luminosity of $L(H_2) = 0.8\ L_\odot$. From a comparison of the H_2 emission regions sampled by the various slit positions with the overall morphology of the H_2 emission in HH135/HH136, it is estimated that the total H_2 luminosity in HH135/HH136 reaches at least 2 $L_\odot$, but possibly exceeds this number by factors of a few. The total H_2 population density, for the two-component mixture assumed above, is $N_{\rm tot}(H_2) = \Sigma_{v'J'} N(v'J') = 77N(1,3)$, or $N_{\rm tot}(H_2) = 5.2 \times 10^{18}$ cm^{-2}. The scaling factors (14.2 and 77 in the present case) are dependent on the actual ro-vibrational population distribution and show a pronounced dependence on the H_2 excitation temperature (e.g., Gredel 1994).

Low-mass stars that power molecular outflows such as HH111 and HH212 have bolometric luminosities of a few tens of solar luminosities (Froebrich 2005), whereas the H_2 luminosities associated with such flows are of the order of 0.1 $L_\odot$. The accretion rates of Class 0 and Class I objects are, purportedly, proportional to the flow luminosities (Stanke 2000; Froebrich et al. 2003), and the H_2 luminosities $L(H_2)$ seem to increase with increasing source luminosities L(bol). The very large luminosity of IRAS 11101-5928 suggests the presence of a deeply embedded, intermediate- or high-mass star in formation. Its luminosity and the luminosity of its H_2 outflow define a data point that is consistent with the regression of $L(H_2)$ with L(bol) from the low-mass protostars. This result may be interpreted in terms of a significantly increased accretion rate in IRAS 11101-5829, that

is, that the intermediate- to high-mass star formation witnessed by HH135/HH136 proceeds via accretion as well, but with significantly increased accretion rates, relative to the accretion rates of low-mass protostars. This interpretation is in agreement with Brooks et al. (2003), who suggested that accretion in the luminous IRAS source IRAS 16547-4247 drives the observed, well-collimated outflow that extends over 1.5 pc. Similarly, Davis et al. (2004) observed a collimated, parsec-scale molecular outflow from IRAS 18151-1208 and concluded that massive protostars drive collimated jets while in their earliest stages of evolution. More studies of intermediate- to high-mass protostars and their outflows are needed to understand if the outflow properties are scaled-up versions of the low-mass counterparts and if high-mass star formation proceeds, in general, via the same physical processes that govern low-mass star formation.

3.4. The atomic emission

The J- and H-band spectra of the various emission line knots in the HH135/HH136 region are dominated by a wealth of strong emission lines from [FeII] and from atomic species such as CI, SII, and NI. Emission from hydrogen recombination lines in the Brackett and Paschen series are detected as well. Optical emission from various ions such as [FeII], [FeIII], [SII], [OI], [OII], [OIII], etc., and from HeI and Hα has been reported by Ogura & Walsh (1992). Emission from [FeII] is generally weak in HII regions and planetary nebulae, but rather strong in supernova remnants and in fast shocks.

A comprehensive analysis of the [FeII] emission in Herbig-Haro flows has been presented by Nisini et al. (2002) and by Hartigan et al. (2004). [FeII] emission lines that arise from a common upper level, such as the $a^6D_{9/2}$–$a^4D_{7/2}$(λ1.257 μm), $a^6D_{7/2}$–$a^4D_{7/2}$(λ1.321 μm), $a^4F_{9/2}$–$a^4D_{7/2}$(λ1.644 μm), and $a^4F_{7/2}$–$a^4D_{7/2}$(λ1.809 μm) lines, can be used to determine the reddening towards the line emitting region. As pointed out by Hartigan et al. (2004), the Einstein A-values of Quinet et al. (1996) are probably more accurate than those of Nussbaumer & Storey (1988) because the former result in a better agreement of the extinction values determined from [FeII] lines, compared to the extinction determined from other methods such as the Balmer decrement. From the line fluxes of the sum spectra tabulated in Tables A.8 and A.9, we infer a visual extinction of A_V = 2.5–2.7 mag using Quinet's oscillator strengths. This is in excellent agreement with the values of 2.8–3.2 mag obtained by Ogura & Walsh (1992) from their optical observations. Nussbaumer's A-values result in visual extinctions of 5.4–5.7 mag, which are too large if compared with the extinction inferred from the optical data. We note, however, that the good agreement between the extinction derived here and the value of Ogura & Walsh (1992) may be fortuitous, as the extinction has been derived from [FeII] fluxes in the J- and H-band spectra, which were taken several years apart, and where positional differences of the various slit positions introduce large uncertainties in the [FeII] line fluxes towards some of the knots in HH135/HH136.

Following Nisini et al. (2002), it is in principle possible to estimate the electron temperature T_e via the [FeII]1.257/Paβ flux ratio. Our values would indicate an electron temperature of about $T_e \approx 3000$ K. This value is, however, highly uncertain and probably wrong altogether, as pointed out by the referee. The FeII/Paβ ratio depends on both the abundance of iron in the gas phase and on the ionisation fraction, two parameters that are not well constrained. In addition, at such low electron temperatures, the [FeII] levels of the observed lines, whose excitation energies are above 10 000 K, are not populated enough to give rise to the observed, strong emission. The low temperature is also not consistent with the fast J-shocks needed to account for the iron presence in the gas form. The [FeII]1.257/[CI]0.98 flux ratio, compared with the [FeII]1.247/Paβ flux ratio, suggests the presence of a very fast J-type shock, with shock velocities around $v_s \approx 100\,\mathrm{km\,s^{-1}}$, assuming a standard gas-phase Fe abundance of Fe/H = 10^{-6}. The [FeII]1.644/1.600 ratios are similar to line ratios observed in other HH objects with [FeII] emission. Ratios of 10–15 prevail towards most of the knots in HH135 and HH136 (cf. Tables A.3 and A.4) and indicate electron densities around $n_e = 4000\ \mathrm{cm^{-3}}$ or somewhat below (cf. Fig. 7 of Nisini et al. 2002). Larger ratios of 20–30 are inferred for knots c and D3, and corresponding electron densities are somewhat below $n_e = 3000\ \mathrm{cm^{-3}}$. Flux ratios of [FeII]1.644/1.533 and [FeII]1.644/1.677 of about 10 for all the knots indicate electron densities of the order of $n_e = 3500\ \mathrm{cm^{-3}}$. The manifold atomic emission lines towards HH135/HH136, together with the low spectral resolution available here, causes a large number of line blends (cf. Figs. 12–16), which prohibits a more comprehensive analysis of the atomic emission.

4. Conclusions

The observations presented above and the main conclusions are summarized as follows:

1. The images obtained in the (1, 0) $S(1)$ line of molecular hydrogen reveal the presence of a well-collimated molecular outflow that extents over a scale of about 1 pc.
2. A number of the H_2 emission line knots are associated with faint, underlying continuum emission.
3. The ro-vibrational excitation temperatures of H_2 of the various knots in the HH135/HH136 flow are remarkably constant, and are well characterized by a narrow range of $T_{ex} = 2000 \pm 200$ K.
4. The molecular part of the shocked gas contains a small fraction of some 0.3% of hot H_2 at a ro-vibrational excitation temperature of $T_{ex} = 5500 \pm 200$ K.
5. Very strong emission lines from [FeII] occur towards various knots in HH135/HH136, and emission from HeI, hydrogen recombination lines, [CI], [SII], and [NII] are present as well. The [FeII] line ratios indicate the presence of a fast J-type shock at a speed of $v_s \approx 100\,\mathrm{km\,s^{-1}}$. Electron densities are of the order of $n_e = 3500$–$4000\ \mathrm{cm^{-3}}$ and electron temperatures are $T_e \approx 3000$ K. A more comprehensive analysis of the atomic emission is hampered by the low spectral resolution and the occurrence of a very large number of line blends.
6. The ro-vibrational population distribution of H_2, together with the presence of strong [FeII] emission, which is spatially displaced from the H_2 emission, indicate that the emission lines arise form in the cooling regions of fast, dissociative J-type shocks, where the [FeII] emission traces the fast, dissociative parts of the shocks and where the H_2 emission emerges from regions of oblique shocks where the shock speeds are lower. The presence of emission from re-forming H_2 molecules in the cooling post-shock region is not ruled out.
7. The large H_2 luminosity of 2 $L_\odot$ suggests that the intermediate- to high-mass protostar that powers the HH135/HH136 outflow forms via a significantly increased

accretion rate, compared to the accretion rates of low-mass protostars.

Acknowledgements. It is a great pleasure to thank Drs. Ogura and Sugitani for enlightening discussions about HH135/HH136 and an invitation to Nagoya City University. The useful comments of the anonymous referee regarding a better presentation of the results and an error in the [FeII] analysis are very much appreciated.

References

Brooks, K. J., Garay, G., Mardones, D., & Bronfman, L. 2003, ApJ, 594, L131
Chrysostomou, A., Lucas, P. W., & Hough, J. H. 2005, in Protostars and Planets V, ed. B. Reipurth, D. Jewitt, & K. Keil, 8147
Davis, C. J., Smith, M. D., Eisloeffel, J., & Davies, J. K. 1999, MNRAS, 308, 539
Davis, C. J., Varricatt, W. P., Todd, S. P., & Ramsay Howat, S. K. 2004, A&A, 425, 981
Flower, D. R., Le Bourlot, J., Pineau des Forêts, G., & Cabrit, S. 2003, MNRAS, 341, 70
Froebrich, D. 2005, ApJS, 156, 169
Froebrich, D., Smith, M. D., Hodapp, K.-W., & Eislöffel, J. 2003, MNRAS, 436, 163
Giannini, T., Nisini, B., Caratti o Garatti, A., & Lorenzetti, D. 2002, ApJ, 570, L33
Giannini, T., McCoey, C., Caratti o Garatti, et al. 2004, A&A, 419, 999
Gredel, R. 1994, A&A, 292, 580
Gredel, R. 1996, A&A, 305, 582
Gredel, R., & Dalgarno, A. 1995, ApJ, 446, 852
Hartigan, P., Raymond, J., & Pierson, R. 2004, ApJ, 614, L69
Le Bourlot, J., Pineau des Forêts, G., Flower, D. R., & Cabrit, S. 2002, MNRAS, 332, 985
Martí, J., Rodríguez, L. F., & Reipurth, B. 1995, ApJ, 449, 184
McCoey, C., Giannini, T., Flower, D. R., & Caratti o Garatti, A. 2004, MNRAS, 353, 813
Nisini, B. C., Caratti o Garatti, A., Giannini, T., & Lorenzetti, D. 2002, A&A, 393, 1035
Nussbaumer, H., & Storey, P. J. 1988, A&A, 193, 327
Ogura, K., & Walsh, J. R. 1992, ApJ, 400, 248
Ogura, K., Nakano, M., & Sugitani, K., & Liljeström, T. 1998, A&A, 338, 576
Pickles, A. J. 1998, PASP, 110, 863
Quinet, P., Le Dourneuf, M., & Zeippen, C. J. 1996, A&AS, 120, 361
Stanke, T. 2000, Ph.D. Thesis, Univ. Potsdam
Steppe, H. 1977, A&AS, 27, 415
Sugitani, K., & Ogura, K. 1994, ApJS, 92, 163
Tamura, M., Hough, J. H., Chrysostomou, A., et al. 1997, MNRAS, 287, 894
Wilgenbus, D., Cabrit, S., Pineau des Forêts, G., & Flower, D. R. 2000, A&A, 356, 1010
Wolniewicz, L., Simbotin, I., & Dalgarno, A. 1998, APJS, 115, 293

Online Material

Appendix A:

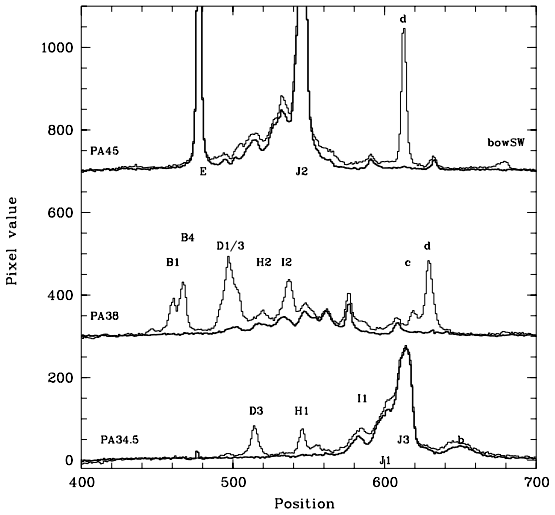

Fig. A.1. Spatial variation of the (1, 0) $S(1)$ H_2 emission line flux along the slit for the three positions PA = 34.5, 38°, and 45° as inferred from the March 1999 observations. Bold lines show the variation of the continuum emission.

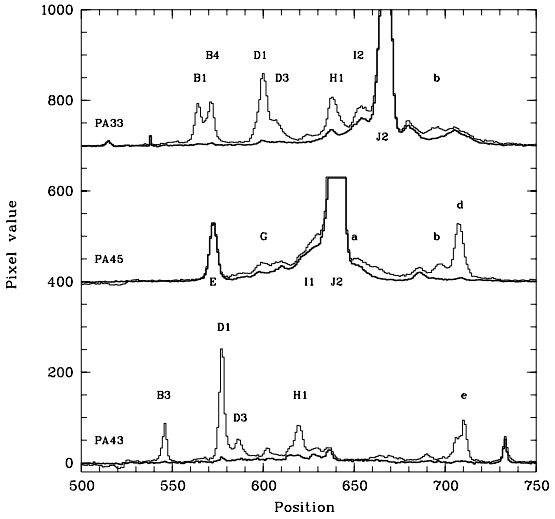

Fig. A.2. Spatial variation of the (1, 0) $S(1)$ H_2 emission line flux along the slit at the three positions PA = 33°, 45°, and 43° as inferred from the February 2004 observations. Bold lines show the variation of the continuum emission.

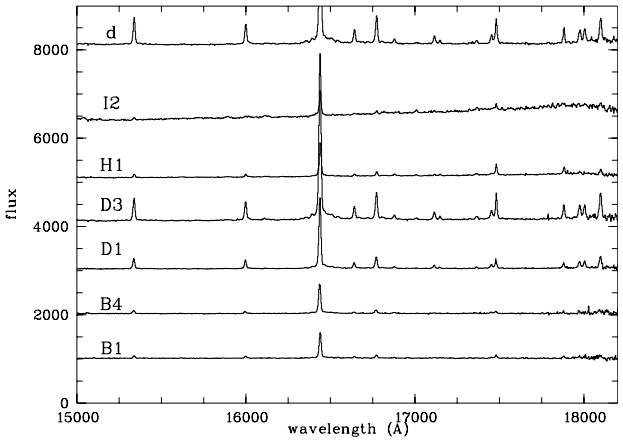

Fig. A.3. *H*-band spectra of individual knots in the HH135 flow. Spectra are shifted by units of 1000, 2000, 3000, 4000, 5000, 6000, and 8000 for knots HH135-B1, B4, D1, D3, H1, I2, and HH136-d, respectively, along the ordinate.

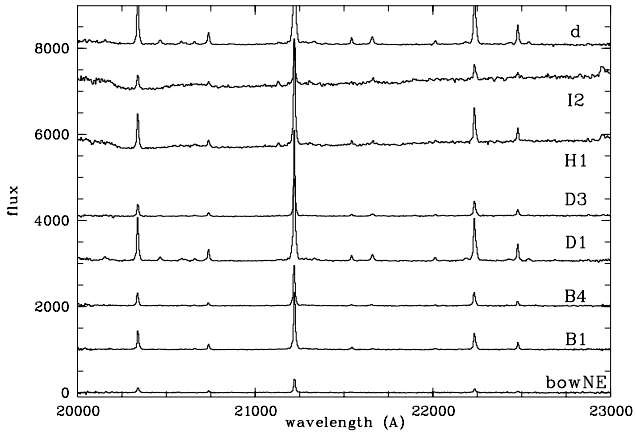

Fig. A.4. *K*-band spectra of individual knots in the HH135 flow. The ordinate is valid for bowNE only. Spectra are shifted by units of 1000, 2000, 3000, 4000, 5000, 6000, and 8000 for knots HH135-B1, B4, D1, D3, H1, I2, and HH136-d, respectively, along the ordinate.

Table A.1. Individual measurements of emission lines towards the various knots in HH135 and HH136, using the low resolution spectra obtained with grism GB.

Wavelength (μm)	Line flux (10^{-20} W m^{-2})									
	*PA*33			*PA*43					*PA*65	
	*B*1	*B*4	*D*1	*B*4	*D*1	*H*1	*e*	*a*	*B*1	*B*2
0.953	0.4	1.4	1.0	0.3	0.6	–	–	3.5	0.6	0.6
0.983	0.2	0.3	0.3	0.1	0.3	0.1	0.3	0.7	0.3	0.3
0.986	0.5	0.9	0.8	0.4	0.6	0.2	0.8	1.9	0.7	0.6
1.006	0.2	0.5	0.6	0.2	0.4	0.2	0.1	1.3	0.4	0.3
1.0293	0.5	1.7	1.8	0.4	1.8	0.1	0.3	4.6	0.7	0.6
1.033	1.3	3.8	4.2	1.1	2.6	0.4	0.8	10.9	1.6	1.5
1.038	0.3	0.8	0.8	0.2	0.8	0.1	0.1	2.0	0.3	0.4
1.041	0.5	1.2	2.1	0.2	1.2	0.2	0.2	4.9	0.4	0.4
1.053	0.1	–	0.4	0.1	–	–	0.1	0.3	–	–
1.064	0.2	0.3	0.2	–	0.1	–	0.2	0.5	–	0.2
1.072	0.2	0.4	0.3	–	–	–	0.2	0.9	0.3	0.2
1.084	3.3	10.2	8.7	3.4	6.8	1.1	1.8	22.7	4.4	3.9
1.095	0.3	1.0	1.1	0.5	1.0	0.4	0.5	2.4	0.4	0.5
1.163	0.2	0.4	0.4	0.1	0.3	0.1	–	0.6	0.3	0.3
1.189	0.4	1.1	1.2	0.4	0.8	0.2	0.3	2.5	0.8	0.6
1.233	0.1	0.2	0.2	0.1	0.2	0.1	0.3	0.5	0.2	0.1
1.239	0.1	0.3	0.3	0.2	0.2	0.1	0.4	0.4	0.3	0.3
1.248	0.3	0.7	0.9	0.3	0.9	0.2	0.3	1.7	0.6	0.5
1.257	8.5	20.0	22.4	7.7	17.1	3.8	5.9	39.5	11.1	9.8
1.271	0.4	1.2	1.5	0.4	1.1	0.1	0.1	2.6	0.5	0.4
1.279	0.7	2.0	2.4	0.9	2.2	0.3	0.2	4.4	0.9	0.7
1.282	0.7	2.4	3.8	0.6	2.8	1.4	1.0	6.3	1.2	1.2
1.295	1.1	2.9	3.7	1.0	2.8	0.5	0.5	6.6	1.4	1.1
1.298	0.3	0.8	0.9	0.2	0.7	0.1	–	1.7	0.3	0.3
1.321	2.5	5.7	7.3	2.2	5.6	1.3	1.8	12.0	3.4	2.9
1.328	0.7	1.8	2.1	0.5	1.6	0.2	0.3	3.7	0.8	0.5
1.534	1.7	4.2	6.6	1.4	4.9	1.1	0.8	8.4	2.0	1.6
1.600	1.2	3.1	5.5	1.0	4.0	0.8	0.6	–	1.5	1.3

[a] Flux uncertainties are 10% in general, but increase to about 50% for $1.10 \leq \lambda \leq 1.18\,\mu$m.

Table A.2. Individual *K*-band measurements of emission lines towards the various knots in HH135 and HH136, using the medium resolution spectra obtained with grism HR.

Wavelength (μm)	Line flux (10^{-20} W m^{-2})													
	*PA*65			*PA*45		*PA*43			*PA*33					
	*B*2	*B*1	*bowNE*	*d*	*c*	*D*1	*D*3	*B*3	*bowNE*	*b*	*H*1	*I*2	*D*1	*B*4	*B*1
2.034	14.2	8.4	2.9	17.0	8.4	21.3	6.6	6.5	2.9	7.6	17.9	–	37.1	12.5	10.7
2.046	0.9	–	–	1.0	0.2	3.6	–	0.3	–	–	–	–	7.8	1.4	–
2.074	2.6	2.1	0.6	2.9	0.8	5.2	1.4	1.1	0.6	1.6	2.9	–	7.3	2.9	2.3
2.122	39.5	26.3	6.8	47.9	21.0	59.2	19.0	19.5	7.3	22.7	48.4	19.6	103.3	36.3	29.9
2.154	1.4	1.0	0.4	1.7	0.8	2.5	0.8	0.5	0.3	1.7	1.0	–	4.0	1.5	1.1
2.166	0.6	0.4	–	0.2	0.5	3.6	1.4	0.7	–	1.2	–	1.5	7.1	1.6	–
2.201	0.7	0.5	0.2	0.5	0.4	1.2	0.3	0.3	0.4	–	0.4	–	1.5	0.9	0.6
2.223	11.1	7.4	1.7	12.5	5.7	20.8	6.6	6.5	1.6	6.6	13.8	5.7	37.7	12.4	8.0
2.247	3.4	2.4	0.6	4.5	3.1	6.6	2.4	1.9	1.0	2.1	4.2	2.3	10.5	3.5	2.9

[a] Flux uncertainties are 10% in general, but increase to about 50% for $\lambda \leq 2.05\,\mu$m.

Table A.3. Individual *H*-band measurements of emission lines towards the various knots in HH135 and HH136, using the medium resolution spectra obtained with grism HR.

Wavelength (μm)	Line flux (10^{-20} W m^{-2})														
	*PA*33			*PA*43				*PA*33			*PA*45		*PA*65	
	*B*1*B*4	*D*1*D*3	*H*1	*B*3	*D*1	*H*1	*e*	*B*4	*D*1	*H*1	*c*	*d*	*B*1	*B*2
1.534	12.5	18.7	1.9	3.6	9.8	3.4	1.9	3.0	8.3	3.1	2.8	23.5	2.0	6.2
1.600	9.3	12.7	1.1	2.3	7.4	1.9	1.2	1.4	5.3	2.1	1.5	15.7	1.7	4.8
1.644	99.3	159.4	24.4	32.2	71.0	30.7	20.9	29.2	64.9	29.5	26.7	155.4	23.4	65.3
1.664	6.4	7.8	0.9	1.9	5.3	1.4	0.7	0.6	3.1	1.3	1.3	10.9	1.2	4.3
1.677	10.5	17.3	2.0	3.2	8.9	2.8	1.5	2.0	7.3	2.6	2.0	19.7	2.1	6.8
1.688	2.0	1.5	1.3	–	2.0	1.5	1.1	0.5	0.6	1.3	1.6	3.5	0.3	1.7
1.712	2.8	3.5	0.7	–	2.2	1.0	0.1	0.2	1.6	0.6	0.6	6.1	0.4	1.3
1.715	1.2	0.6	–	–	0.6	0.6	0.7	–	0.3	0.5	1.0	2.2	–	0.7
1.736	–	–	–	–	–	–	–	–	–	–	–	2.4	–	–
1.745	2.3	4.5	–	–	2.5	0.6	0.3	–	2.4	0.8	–	6.9	0.6	2.1
1.748	11.0	12.6	3.6	2.2	5.4	5.5	5.6	1.3	4.3	5.5	6.5	14.2	2.0	6.9
1.788	5.9	6.8	–	–	2.8	3.6	3.8	–	2.3	6.0	4.1	7.2	1.2	4.2
1.798	4.8	5.5	–	–	3.8	–	–	–	3.2	3.3	0.5	5.7	–	3.4
1.800	1.8	0.6	–	–	3.8	–	–	–	0.8	–	–	4.1	–	2.6
1.810	5.6	9.5	–	–	5.6	–	–	–	4.2	–	–	8.1	–	4.3

[a] Flux uncertainties are 10% in general.

Table A.4. Individual *H*-band measurements of emission lines towards the various knots in HH135 and HH136, using the low resolution spectra obtained with grism GR.

Wavelength (μm)	Line flux (10^{-20} W m^{-2})														
	*PA*38						*PA*45	*PA*65		*PA*34.5			*PA*34.5		
	*D*1	*B*1	*B*4	*D*1	*d*	*c*	*d*	*bowNE*	*B*2	*D*3	*H*1	*b*	*D*3	*H*1	*b*
1.534	4.3	2.8	8.0	11.6	20.2	0.5	15.0	0.2	4.5	0.9	–	–	1.2	3.0	0.1
1.600	3.0	1.8	5.5	8.7	14.2	0.3	11.1	–	3.6	0.5	–	–	0.4	1.9	–
1.644	27.3	18.6	54.0	91.7	112.2	8.4	82.8	2.4	36.7	9.3	6.8	3.3	12.1	25.0	2.2
1.664	1.6	0.8	3.5	5.0	7.4	–	6.1	–	1.7	0.3	–	–	0.4	0.9	–
1.678	3.3	1.8	6.1	10.7	15.2	0.6	11.4	0.2	3.8	–	–	–	0.7	2.3	–
1.712	0.8	0.4	1.4	2.3	4.3	0.1	3.0	0.2	1.0	0.2	–	–	0.2	0.7	–
1.748	3.7	3.3	7.9	12.1	18.3	2.0	14.9	1.2	4.7	1.9	–	–	1.6	6.4	1.2
1.789	1.4	1.7	3.2	5.8	5.3	1.4	6.3	0.7	1.8	0.8	–	–	2.2	5.1	1.9
1.798	3.1	1.5	4.8	13.2	13.2	1.4	9.4	0.4	3.9	2.5	–	–	5.6	5.2	–
1.810	21.0	14.9	34.8	76.9	85.7	6.0	72.3	2.2	26.7	10.8	–	–	15.5	17.5	–
1.958	22.0	24.3	37.8	74.6	84.3	8.4	81.9	7.4	22.5	7.7	–	–	8.6	36.6	–
2.034	4.7	5.5	10.3	19.8	18.4	2.8	17.2	1.7	7.2	2.9	5.7	2.9	6.4	14.2	5.8
2.047	0.7	–	–	–	–	–	5.6	–	0.4	–	–	–	0.7	–	–
2.074	0.7	0.9	2.0	2.8	2.6	–	3.4	0.3	1.3	0.2	–	–	–	5.5	–
2.122	12.1	14.5	29.9	53.0	48.5	7.2	47.1	3.8	19.1	7.1	10.4	7.3	12.4	27.7	12.7
2.155	0.5	0.6	1.2	1.9	3.2	0.7	1.0	0.3	0.6	0.2	–	–	0.5	1.7	–
2.167	1.1	–	0.8	3.3	4.1	0.3	1.4	–	–	0.4	–	–	0.7	2.9	–
2.202	0.3	0.3	0.7	1.1	1.3	0.3	0.8	0.2	–	–	–	–	–	–	–
2.224	4.3	4.5	9.7	18.4	17.6	2.1	14.9	1.2	5.8	2.4	4.0	3.2	4.9	8.5	3.7
2.248	1.3	1.6	3.0	5.6	6.0	1.0	4.9	0.6	1.5	1.0	1.9	1.6	2.0	3.7	1.3
2.355	1.3	0.5	0.7	1.9	2.2	0.4	1.7	0.5	0.5	0.6	–	–	–	–	–
2.406	13.5	15.4	31.1	58.9	50.9	7.7	53.3	4.1	21.6	8.9	13.1	7.9	16.4	26.7	15.3
2.413	5.8	8.7	15.2	36.5	25.8	4.0	26.8	2.0	10.0	4.1	6.3	4.3	7.9	12.3	7.6
2.423	14.0	15.4	31.6	59.2	50.9	7.2	53.1	4.1	21.0	7.2	12.4	9.1	13.8	29.2	16.7
2.437	–	5.0	9.0	16.9	15.3	3.3	17.6	1.5	6.2	2.4	–	–	–	–	–
2.453	–	–	1.3	–	–	–	4.5	–	2.3	–	–	–	–	–	–
2.475	–	2.1	3.8	12.9	4.9	–	4.9	–	–	–	–	–	–	–	–
2.498	–	3.7	9.7	25.4	12.5	–	12.5	–	–	–	–	–	–	–	–

[a] Flux uncertainties are 10% in general, but increase to about 50% for $1.9 \leq \lambda \leq 2.05$ μm and for $\lambda \geq 2.43$ μm.

Table A.5. H_2 line fluxes and column densities in ro-vibrational levels $v'J'$, as measured from the low-resolution sum spectrum obtained with the blue grism GB.

Line transition	Wavelength μm	Flux 10^{-20} W m^{-2}	$N(v'J')$ 10^{14} cm^{-2}
(2, 0)S(9)	1.054	156	7(1)
(2, 0)S(7)	1.064	128	5(1)
(2, 0)S(6)	1.073	141	6(1)
(2, 0)S(4)	1.100	82	4(1)
(2, 0)S(3)	1.117	379	19(10)
(2, 0)S(2)	1.138	225	14(7)
(3, 1)S(5)	1.152	188	4(2)
(2, 0)S(1)	1.162	288	22(11)
(3, 1)S(4)	1.167	55	1(0.5)
(3, 1)S(3)[a]	1.186	170	4(1)
(4, 2)S(9)	1.196	62	1(0.5)
(4, 2)S(8)	1.199	59	1(0.5)
(4, 2)S(7)	1.205	67	1(0.5)
(4, 2)S(2)	1.285	56	1(0.5)
(4, 2)S(6)	1.214	27	0.4(0.2)
(4, 2)S(5)	1.226	69	1(0.5)
(3, 1)S(1)	1.233	156	5(1)
(2, 0)Q(2)	1.242	95	11(2)
(2, 0)Q(3)	1.247	465	57(11)
(2, 0)Q(4)	1.255	251	32(6)
(2, 0)Q(5)	1.264	420	55(11)
(2, 0)Q(7)	1.287	114	16(3)
(3, 1)Q(1)	1.314	138	5(1)
(4, 2)S(1)	1.312	125	3(1)

[a] Possible blend with [PI].

Table A.6. H_2 line fluxes and column densities in ro-vibrational levels $v'J'$, as measured from the low-resolution sum spectrum obtained with the red grism GR.

Line transition	Wavelength μm	Flux 10^{-20} W m^{-2}	$N(v'J')$ 10^{14} cm^{-2}
(1, 0)S(9)	1.688	510	65(13)
(1, 0)S(8)	1.715	700	65(13)
(1, 0)S(7)	1.748	2798	207(41)
(1, 0)S(3)	1.958	17948	1056(528)
(1, 0)S(2)	2.034	3016	195(97)
(2, 1)S(3)	2.074	897	41(20)
(1, 0)S(1)	2.122	8657	669(134)
(2, 1)S(2)	2.154	416	20(4)
(1, 0)S(0)	2.223	2599	289(58)
(2, 1)S(1)	2.248	521	30(6)
(1, 0)Q(1)	2.407	10675	757(454)
(1, 0)Q(2)	2.413	6122	616(370)
(1, 0)Q(3)	2.424	8936	984(590)
(1, 0)Q(4)	2.437	4419	514(308)

Table A.7. H_2 line fluxes measured from the medium-resolution *H*- and *K*-band sum spectra obtained with the HR grism in orders 4 and 3, respectively.

Line transition	Wavelength μm	Flux 10^{-20} W m^{-2}	$N(v'J')$ 10^{14} cm^{-2}
(1, 0)*S*(9)	1.688	652	83(17)
(1, 0)*S*(8)	1.715	278	26(5)
(1, 0)*S*(7)	1.748	2328	172(34)
(1, 0)*S*(6)	1.788	1504	96(19)
(1, 0)*S*(2)	2.034	2977	192(96)
(3, 2)*S*(5)	2.066	198	11(6)
(2, 1)*S*(3)	2.074	623	28(14)
(1, 0)*S*(1)	2.122	8763	677(135)
(2, 1)*S*(2)	2.154	371	18(4)
(3, 2)*S*(3)	2.201	159	8(2)
(1, 0)*S*(0)	2.223	2901	323(65)
(2, 1)*S*(1)	2.248	970	55(11)

Table A.8. Line fluxes measured for atomic transitions using the low-resolution spectrum obtained with grism GB.

Transition	Wavelength μm	Flux 10^{-20} W m^{-2}
$^1D_2$–$^3P_2$ SIII	0.953	839
FeII?	0.955	177
$^1D_2$–$^3P_1$ CI	0.983	179
$^1D_2$–$^3P_2$ CI	0.985	678
H 7–3	1.005	340
?	1.019	62
$^2P_{3/2}$–$^2D_{3/2}$ SII	1.029	1019
$^2P_{3/2}$–$^2D_{5/2}$ SII	1.033	2497
$^2P_{1/2}$–$^2D_{5/2}$ SII	1.038	413
$^2P_{1/2}$–$^2D_{5/2}$ NI	1.041	1019
HeI	1.083	5516
H 6–3	1.094	616
^5P–$^5S_0$ OI	1.130	195
?	1.134	192
?	1.144	59
PII	1.147	116
?	1.149	39
?	1.176	58
$a^6D_{9/2}$–$a^4D_{5/2}$ FeII	1.191	143
$a^6D_{9/2}$–$a^4D_{7/2}$ FeII	1.257	11134
$a^6D_{1/2}$–$a^4D_{1/2}$ FeII	1.271	684
$a^6D_{3/2}$–$a^4D_{3/2}$ FeII	1.279	1132
H 5–3	1.282	1645
$a^6D_{5/2}$–$a^4D_{5/2}$ FeII	1.294	1650
$a^6D_{7/2}$–$a^4D_{7/2}$ FeII	1.321	3595
$a^6D_{3/2}$–$a^4D_{5/2}$ FeII	1.328	1083
$a^4F_{9/2}$–$a^4D_{5/2}$ FeII	1.533	2439
$a^4F_{7/2}$–$a^4D_{3/2}$ FeII	1.600	1866

Table A.9. Wavelengths and line fluxes of atomic transitions, derived from spectra obtained with grisms GR and HR in orders 4 and 3, respectively.

Transition	Wavelength μm	Flux 10^{-20} W m^{-2}
$a^4F_{9/2}$–$a^4D_{5/2}$ FeII	1.534	2459
$a^4F_{7/2}$–$a^4D_{3/2}$ FeII	1.600	1380
H 12–4	1.641	200
$a^4F_{9/2}$–$a^4D_{7/2}$ FeII	1.644	13521
$a^4F_{5/2}$–$a^4D_{1/2}$ FeII	1.664	563
$a^4F_{7/2}$–$a^4D_{5/2}$ FeII	1.677	1512
H 11–4	1.681	568
$^3P_0$ –^{3} D HeI	1.700	176
H 10–4	1.737	972
H 7–4	2.166	1191
$a^4F_{9/2}$–$a^4D_{5/2}$ FeII	1.533	2637
$a^4F_{7/2}$–$a^4D_{3/2}$ FeII	1.600	2130
$a^4F_{9/2}$–$a^4D_{7/2}$ FeII	1.644	13830
$a^4F_{5/2}$–$a^4D_{1/2}$ FeII	1.664	1356
$a^4F_{5/2}$–$a^4D_{5/2}$ FeII	1.677	2597
H 10–4	1.736	620
$a^4F_{3/2}$–$a^4D_{1/2}$ FeII	1.745	1295
$a^4F_{3/2}$–$a^4D_{3/2}$ FeII	1.797	1017
$a^4F_{5/2}$–$a^4D_{5/2}$ FeII	1.800	1301
$a^4F_{7/2}$–$a^4D_{7/2}$ FeII	1.809	2173
H 7–4	2.166	613